Title

Rational Design of Fluorinated Electrolytes for Low Temperature Lithium-Ion Batteries



Journal

Advanced Energy Materials, 13(20)

ISSN

1614-6832

Authors

Yoo, Dong-Joo

Liu, Qian

Cohen, Orion

et al.

Publication Date

2023-05-01

DOI

10.1002/aenm.202204182

ADVANCED ENERGY MATERIALS
www.advenergymat.de

# Rational Design of Fluorinated Electrolytes for Low Temperature Lithium-Ion Batteries

*Dong-Joo Yoo, Qian Liu, Orion Cohen, Minkyu Kim, Kristin A. Persson,* and Zhengcheng Zhang**

**Nonaqueous carbonate electrolytes are commonly used in commercial lithium-ion battery (LIB). However, the sluggish $Li^+$ diffusivity and high interfacial charge transfer resistance at low temperature (LT) limit their wide adoption among geographical areas with high latitudes and altitudes. Herein, a rational design of new electrolytes is demonstrated, which can significantly improve the low temperature performance below −20 °C. This electrolyte is achieved by tailoring the chemical structure, i.e., altering the fluorination position and the degree of fluorination, of ethyl acetate solvent. It is found that fluorination adjacent to the carbonyl group or high degree of fluorination leads to a stronger electron-withdrawing effect, resulting in low atomic charge on the carbonyl oxygen solvating sites, and thus low binding energies with $Li^+$ ions at LT. The optimal electrolyte 2,2,2-trifluoroethyl acetate (EA-f) shows significantly improved cycle life and C-rate of a NMC622/graphite cell when cycled at −20 °C and −40 °C, respectively. In addition to superior LT performance, the electrolyte is nonflammable and tolerant for high voltage charging all owing to its fluorine content. This work provides guidance in designing next-generation electrolytes to address the critical challenge at subzero temperatures.**

## 1. Introduction

Lithium-ion batteries (LIBs) are exploited in most portable electronics because of high energy/power density (long operation time), cyclability (life span), and simple manufacturing process (mass production).[1–4] However, with the spread of electric vehicles, low temperature operation of LIBs has become an issue due to the performance difference depending on regions and seasons.[5,6] Low temperature performance is considered to be the most challenging aspect in LIBs because the conventional electrolytes are based on ethylene carbonate (EC), an indispensable electrolyte solvent for stable solid-electrolyte-interphase (SEI) that also exhibits a high melting point of 34 °C.[7,8] As temperatures drop, EC-based LIBs suffer from sharp drops in capacity and rate capability and severe degradation at low temperatures.[7,8]

The electrolytes in LIBs with graphite anodes normally include specific ratio of EC solvent since it can stabilize the graphite/electrolyte interface by ring-opening reduction, preventing the graphite from exfoliation by co-intercalation.[9,10] However, the high melting point (34 °C) of EC impairs the low temperature performances as the electrolytes with a high portion of EC freeze under −20 °C. To address the freezing problem, tertiary or quaternary carbonate systems with a low portion of EC were proposed,[11,12] but they still suffered from poor rate capability at low temperatures. In addition, to enhance rate capability at low temperatures, solvents with a high ionic conductivity such as ether,[13–18] ester,[19–25] or nitrile[8,26,27] have been attempted as cosolvents. Among the functional groups, ester-based solvents have been actively studied due to the similar functionality with carbonates, but much lower melting points.

Recently, in the battery field, fluorinated electrolytes have received a tremendous attention from researchers due to their unexpected superior properties such as high oxidation stability, stable interface formation, and weak solvation energy.[28–30] Although some fluorinated ester-based electrolytes[31–34] such as methyl 3,3,3-trifluoropionate, or ethyl trifluoroacetate were proposed for LIBs at low temperatures, the behind working mechanisms remain ambiguous. Previous studies on fluorinated ester electrolytes have studied the conventional

D.-J. Yoo, Q. Liu, M. Kim, Z. Zhang
Chemical Sciences and Engineering Division
Argonne National Laboratory
Lemont, IL 60439, USA
E-mail: zzhang@anl.gov

O. Cohen
Department of Chemistry
University of California Berkeley
Berkeley, CA 94720, USA

K. A. Persson
Department of Materials Science and Engineering
University of California Berkeley
Berkeley, CA 94720, USA
E-mail: kapersson@lbl.gov

K. A. Persson
The Molecular Foundry
Lawrence Berkeley National Laboratory
Berkeley, CA 94720, USA

The ORCID identification number(s) for the author(s) of this article can be found under https://doi.org/10.1002/aenm.202204182.



**DOI: 10.1002/aenm.202204182**

electron-withdrawing effects of fluorination but provided little insight into the relation between the molecular structure and electrochemical performances.

In this paper, we systematically investigate the effect of the position and degree of fluorination on ethyl acetate (EA) as an electrolyte solvent. The terminal methyl groups of EA were replaced by trifluoro methyl groups, and compared from the view of physical, chemical, and electrochemical properties. We thoroughly analyzed their ionic conductivities, solvation structures ($^{7}$Li and $^{19}$F-nuclear magnetic resonance (NMR)), reduction potential (from density functional theory (DFT) and molecular dynamics (MD) simulations), solid-electrolyte interphase (SEI) layer, interfacial resistances, and electrochemical performances. From the various characterizations, we found an unexpected correlation:solvents fluorinated closer to the ester group possess poor physical properties such as low solubilities, ion clustering, and low ionic conductivities from extremely low binding energies. This defies the conventional understanding that weak solvation energy induced by fluorination is beneficial for improved electrochemical performances. Instead, the weakened physical properties impose a large overpotential during operation at low temperatures. This paper provides novel insights on design principles of fluorinated electrolytes for high-performance LIBs at low temperatures.

## 2. Results and Discussion

### 2.1. Design Principle of Fluorinated Ester-Based Electrolytes

Compared with the conventional Gen 2 electrolytes with ethylene carbonate and ethyl methyl carbonate cosolvent (1.2 M $LiPF_6$ in EC/EMC w/w = 3/7), the state-of-the-art electrolyte for low temperature performances includes ethyl acetate (EA) solvent with fluoroethylene carbonate (FEC) cosolvent (**Figure 1**a). We reconfirmed the superiority of EA solvent compared with ethyl butyrate (EB) solvent (Figure S1, Supporting Information) and the stable SEI layer formation of FEC cosolvent by comparing pure EA, EA/EC (9/1), and EA/FEC (9/1) electrolytes (Figure S2, Supporting Information). Although EA has a low melting point and high ionic conductivity, it exhibits a stronger binding to $Li^+$ ions than EMC due to the absence of an electron-withdrawing ester group, resulting in a higher desolvation energy. To decrease the desolvation energy, one of the limiting factors of $Li^+$ ion kinetics at low temperatures, we functionalized the terminal methyl group ($-CH_3$) to trifluoro methyl group ($-CF_3$), a strong electron-withdrawing group. In addition, the fluorination enhances high voltage stability with reduced highest occupied molecular orbital (HOMO) levels, preventing the possible oxidation of hydrogen at high voltage. Moreover, the fluorination of EA provides nonflammable properties to electrolytes (FigureS3, Supporting Information). All the physical properties of solvents we used for this paper are included in Table S1 (Supporting Information).

In order to investigate the effect of the position and degree of fluorination, we compared different types of fluorinated ester solvents including trifluoroethyl acetate (EA-f), ethyl trifluoroacetate (f-EA), and trifluoroethyl trifluoroacetate (f-EA-f) (Figure 1b). Atomic charge analysis via density functional theory (DFT) calculations reveals the electron-withdrawing effect of the $-CF_3$ groups. The atomic charge on the carbonyl group decreases in an order of EA, EA-f, f-EA, and f-EA-f. Since the electron-withdrawing effect in EA-f is shielded by an ether group, EA-f showed a higher atomic charge of –0.583 eV than that of –0.547 eV in f-EA. In the case of f-EA-f, it showed the lowest atomic charge of –0.530 eV due to the high degree of fluorination. This atomic charge analysis suggests different binding energies with $Li^+$ ions and different solvation structures in electrolytes.

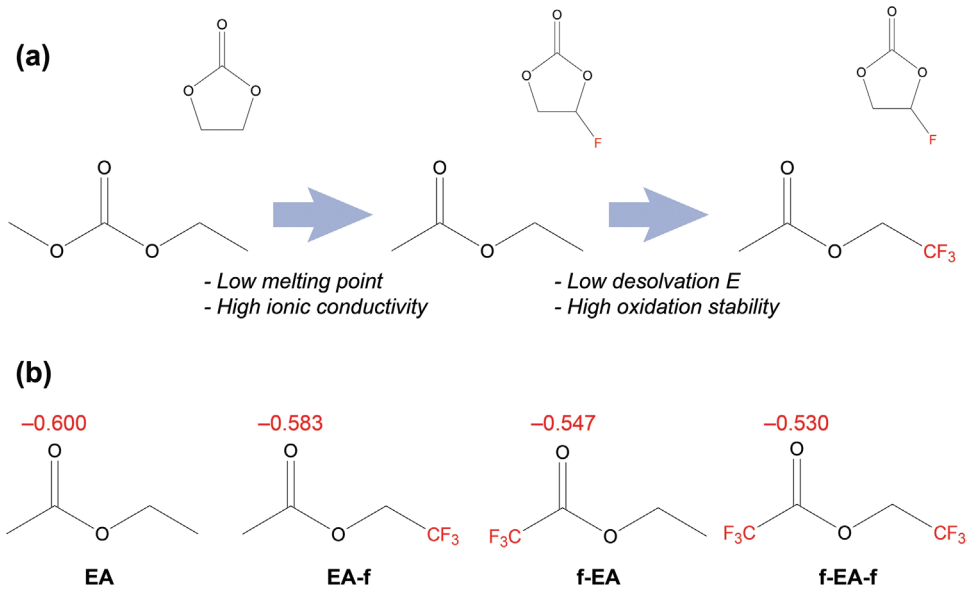


**Figure 1.** a) Scheme of solvent design transition from carbonates to fluorinated esters. b) Atomic charge analysis of carbonyl groups in EA, EA-f, f-EA, and f-EA-f.

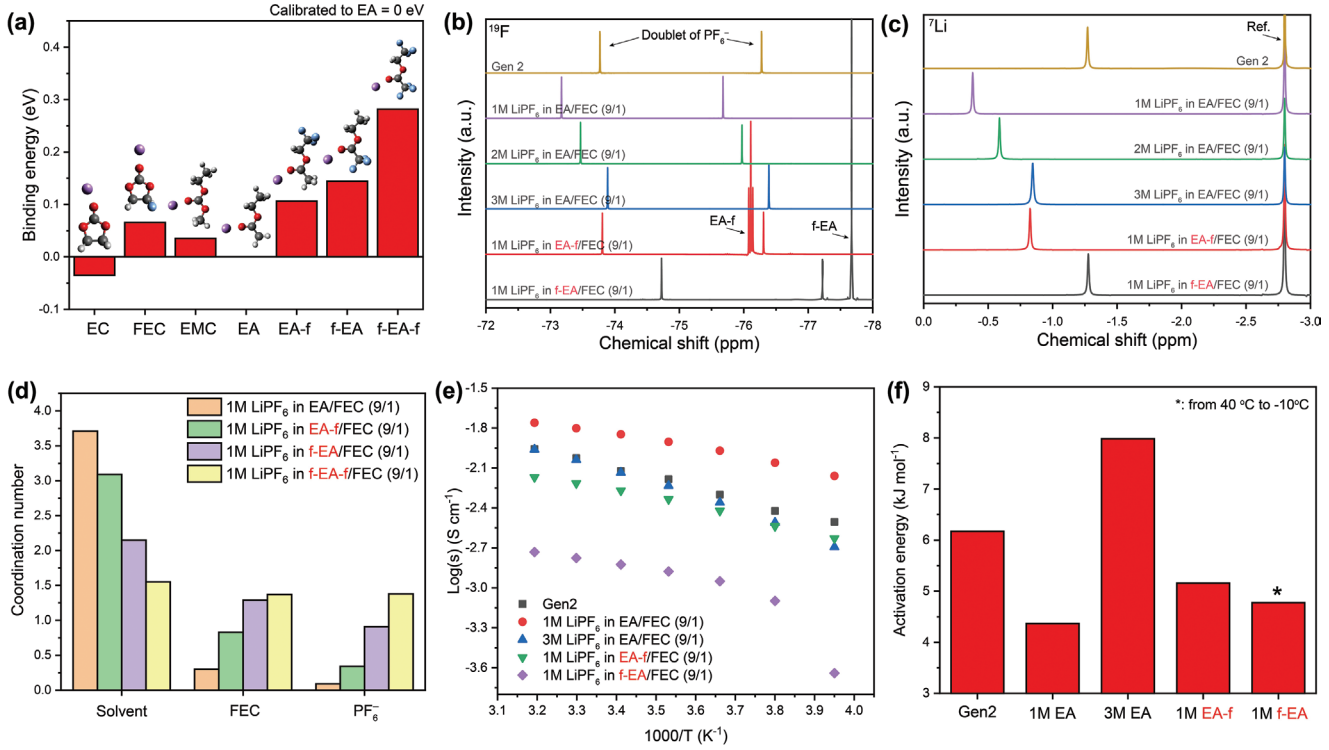


**Figure 2.** a) Binding energies of each solvent with Li ion. The dielectric constant for implicit solvation model was 6.02, and they were calibrated to EA = 0 eV. b) $^{19}$F- and c) $^{7}$Li-NMR spectra of different electrolytes. d) Coordination number in Li solvation sheath of different electrolytes from MD simulation. e) Ionic conductivities of different electrolytes at various temperatures, and f) their calculated activation energies ($E_a$) from plots (e).

### 2.2. Solvation Structures and Ionic Conductivities

To further appreciate the different electron-withdrawing effect, we calculated binding energies of each solvent with a $Li^+$ ion (**Figure 2**a). We applied implicit solvation effect for the calculations because $Li^+$ ions were chelated by f-EA and f-EA-f in gas phase, which is not feasible in electrolytes (Figure S4, Supporting Information). The dielectric constant for implicit solvation effect was 6.02, and they were calibrated to EA = 0 eV. Although each solvent has a different dielectric constant, same value was used to compare their relative binding energies in same surrounding condition. Note that a higher binding energy means relatively weaker binding to a Li ion. FEC had a higher binding energy (0.06 eV) than EC (–0.03 eV) due to the fluorination effect. In the case of EA derivatives, EA-f, f-EA, and f-EA-f showed much higher binding energies of 0.11, 0.14, and 0.28 eV, respectively, than 0 eV of EA. The relative binding energies allow to expect solvation structures in cosolvent systems in a way that solvent with lower binding energy would aggressively solvate Li ions. It is noteworthy that while FEC has a higher binding energy than EA, EA derivatives have higher binding energies than FEC. A weaker interaction between $Li^+$ and the solvent correlates with a higher participation of FEC in the Li solvation shell in EA-derivative electrolytes; however, the interaction between the cosolvents as well as entropic effects can influence the speciation of the Li solvation.

Understanding solvation structures in electrolytes is important because solvents coordinated with Li are likely to be reduced to form the SEI layer. The degree of ion-pairing also affects solubility and ionic conductivity. We used FEC cosolvent with 10 vol% since pure EA or EA-f solvents cannot stabilize the SEI layer (Figure S5, Supporting Information). To analyze the solvation structures, we conducted nuclear magnetic resonance (NMR) characterization for each electrolyte. To note, it is reported that Gen 2 has a high degree of contact ion pairs and aggregates due to the mixing of cyclic and linear carbonates.[35] From the $^{19}$F-NMR spectra in Figure 2b, the doublet of $PF_6^-$ in 1 M $LiPF_6$ in EA/FEC (9/1) (EA electrolyte) was down-field shifted compared with Gen 2, indicating a lower ion-pair ratio. The peaks of $PF_6^-$ were gradually up-field shifted as the concentration increased, showing ion-clustering at high concentrations. While the peaks of $PF_6^-$ in 1 M $LiPF_6$ in EA-f/FEC (9/1) (EA-f electrolyte) were comparable to those in 3 M EA electrolyte or Gen 2, the peaks of $PF_6^-$ in 1 M $LiPF_6$ in f-EA/FEC (9/1) (f-EA electrolyte) were the most up-field shifted. f-EA-f electrolytes could not be measured because 1 M $LiPF_6$ was not soluble in f-EA-f/FEC (9/1) solvent even at room temperature.

The trend of peak shift was continued in the $^{7}$Li-NMR spectra (Figure 2c). As Li ions are solvated by solvents and anions, the corresponding Li peak shift can be considered as the sum of solvent and anion effects. Compared with –1.27 ppm in Gen 2, the Li peak in EA electrolyte was significantly down-field shifted to –0.39 ppm, implying a low portion of $PF_6^-$ in solvation structures. As the concentration increased, the Li peaks were up-field shifted due to the participation of $PF_6^-$ in solvation structures. The Li peak in EA-f electrolyte was comparable to 3 M EA electrolyte, and they were still significantly down-field shifted to –0.82 ppm compared with Gen 2, indicating the weak binding

of EA-f to $Li^+$ ions. The Li peak in f-EA electrolyte was similar to Gen 2 because of the sum of high portion of ion-pair and weak binding of f-EA. The solvation structure modification was reconfirmed by molecular dynamics (MD) simulations (Figure 2d). There is a strict trend in coordination number changes. In an order of EA, EA-f, f-EA, and f-EA-f, the coordination number of EA-derivative solvents decreased, and those of FEC or $PF_6^-$ increased due to the weakened binding energies of EA-derivative solvents. The representative solvation structures of each electrolyte were presented in Figure S6 (Supporting Information). This NMR characterization and MD simulation explain the modified solvation structures and energies in the EA-derivative electrolytes.

Ionic conductivities on various temperatures of different electrolytes were measured by electrochemical impedance spectroscopy (EIS) characterization using bulk electrolytes (Figure 2e,f). As known in the literature, the EA electrolyte had higher ionic conductivity than Gen 2, due to its lower viscosity and lower ion-pair ratio (high dissociation). As the concentration increased to 3 M, the ionic conductivities decreased with a high activation energy of 8.0 kJ $mol^{-1}$ because of the increased ion-pair ratio. In the case of EA-f electrolyte, the ionic conductivities were slightly lower than Gen 2, but they were high enough above 2.4 mS $cm^{-1}$ to sustain ion transport at low temperatures. In the case of f-EA electrolytes, however, the ionic conductivity was significantly low to 1.5 mS $cm^{-1}$ at room temperature, and it dropped to 0.2 mS $cm^{-1}$ at −20 °C because $LiPF_6$ salt in electrolytes was precipitated such a low temperature (Figure S7, Supporting Information). This confirmed that weak binding energy of fluorinated solvents leads to trade-offs between desirable physical properties.

### 2.3. SEI Layers and Interfacial Resistance

In our previous paper, we unveiled that the SEI layer plays a crucial role in rate capability and stability at low temperatures.[8] With that in mind, we added 0.1 M LiDFOB to EA-f electrolyte as an additive to modify the SEI layer. The effect of LiDFOB additive was verified in dQ/dV analysis and the concentration was optimized from the rate capability test results (Figure S8, Supporting Information). The optimized electrolyte was 0.9 M $LiPF_6$ + 0.1 M LiDFOB in EA-f/FEC (9/1). The SEI layer formation can be seen in dQ/dV profiles of NMC622/graphite cells at the first charging step. In **Figure 3**a, there was an EC reduction peak at 3.0 V in Gen 2. While there was a free FEC reduction peak at 2.7 V in EA electrolyte, $Li^+$-coordinated FEC was reduced earlier at 2.3 V in EA-f electrolyte. This is well matched with the coordination number change of FEC in electrolytes from MD simulations. In the EA-f electrolyte with LiDFOB additive, $DFOB^-$ was reduced earlier than $Li^+$-coordinated FEC, forming an ion-conductive SEI layer.[36,37] In the case of f-EA electrolyte, f-EA solvent was reduced earlier than FEC and showed high peaks at 2.6 and 2.7 V due to the high reduction potential (Figure S9, Supporting Information).

To analyze the composition of SEI layers, we conducted X-ray photoelectron spectroscopy (XPS) characterization of graphite anodes after three formation cycles. Based on the atomic ratio in Figure 3b, we observe that the prevalence of Li and O were

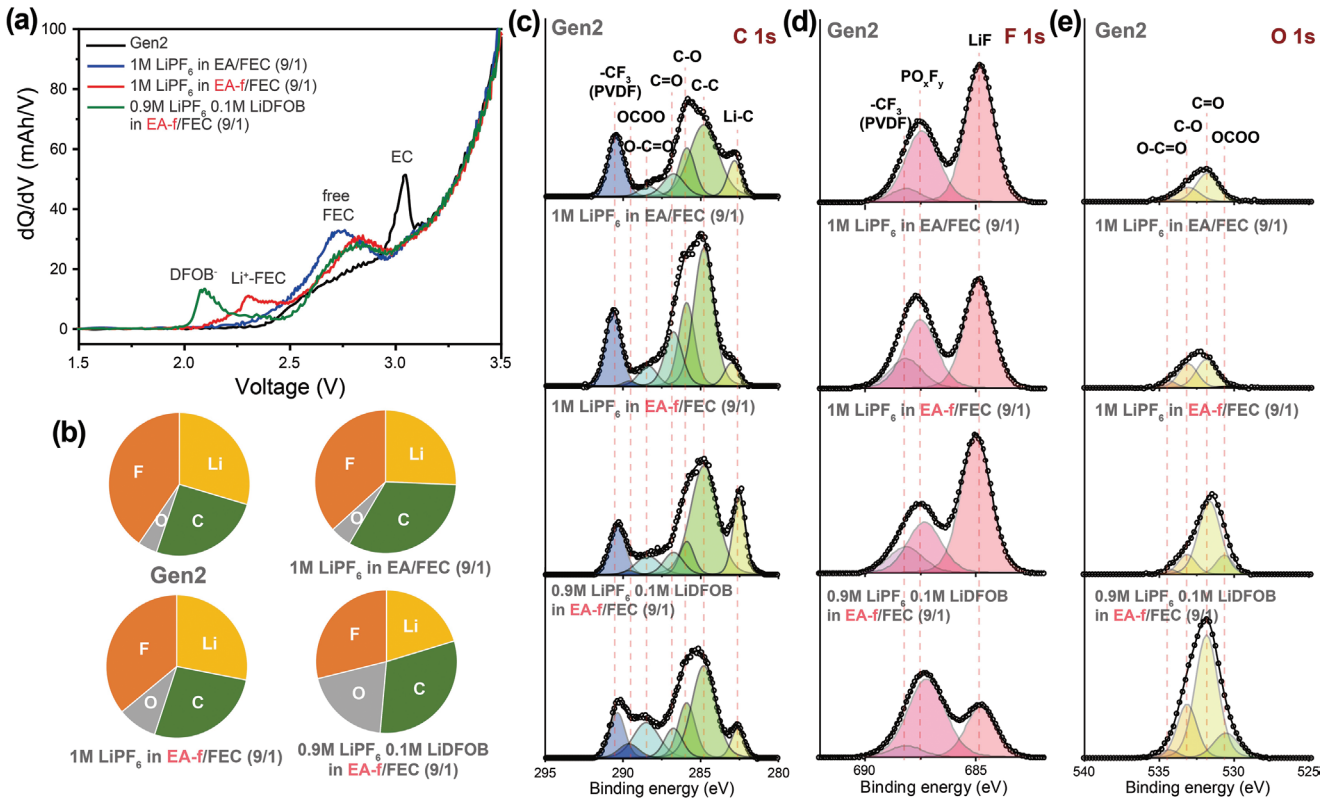


**Figure 3.** a) dQ/dV profiles of graphite|NMC622 cells with different electrolytes during the 1st charging. b) Atomic ratio and XPS spectra of: c) C 1s, d) F 1s, and e) O 1s of cycled graphite anodes after three formation cycles with different electrolytes.

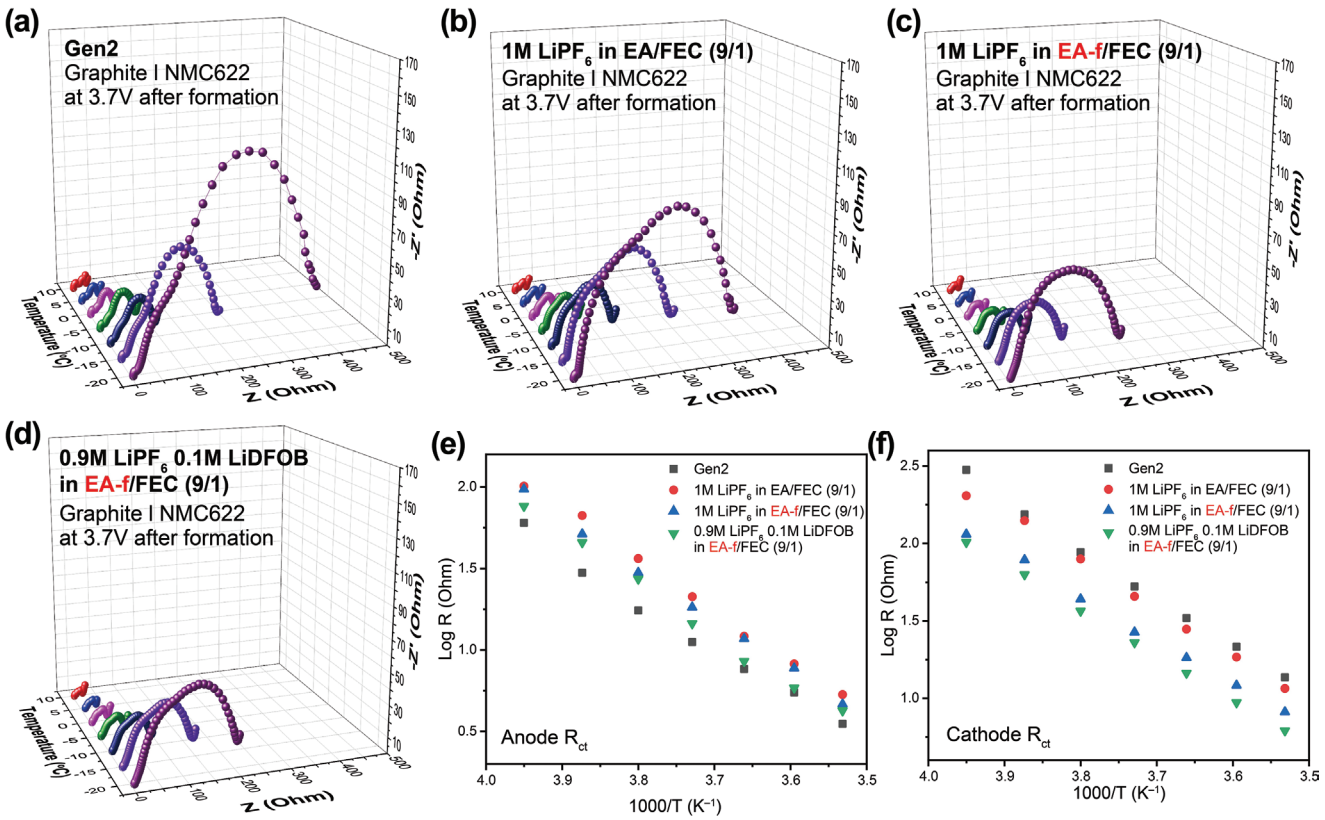


**Figure 4.** Nyquist plots of graphite|NMC622 cells with: a) Gen 2, b) 1 M $LiPF_6$ in EA/FEC (9/1), c) 1 M $LiPF_6$ in EA-f/FEC (9/1), and d) 0.9 M $LiPF_6$ 0.1 M LiDFOB in EA-f/FEC (9/1) electrolyte at various temperatures. Arrhenius plots of: e) $R_{ct\text{-}anode}$, and f) $R_{ct\text{-}cathode}$ fitted from (a–d).

higher in the EA-f electrolyte than EA electrolytes, likely due to the reduction of $Li^+$-coordinated FEC. The fraction of O and C were further enlarged in EA-f electrolyte with LiDFOB additive, correlating to the active reduction of $DFOB^-$. Deconvolution of each element in the XPS spectra clarified the functional groups of reduction products. The participation of $Li^+$-coordinated FEC in the EA-f electrolyte caused a large peak from the C=O bond at 532 eV in O 1s spectra. The addition of LiDFOB further modified the SEI layer, leading to less LiF and more organic compounds, exhibiting C=O, OCOO, and O−C=O bonds. It is reported that the SEI layer formed by LiDFOB additive is composed of polymeric compounds, enabling a lower interface resistance.[38,39] In the case of cathodes in the different electrolytes, there was no significant difference in the components on the surface (Figure S10, Supporting Information).

To appreciate the effect of SEI layer and modified solvation structures to interfacial resistance, we measured temperature-dependent electrochemical impedance spectroscopy (EIS) for NMC622/graphite cells charged to 3.7 V after three formation cycles (**Figure 4**). It is evident that as the temperature decreased, the total resistances increased due to the lower thermal energy of $Li^+$ ions for electrochemical reactions. While Gen 2 and EA electrolytes showed large total resistance of 365 and 315 Ω at −20 °C, respectively, EA-f electrolyte showed a much lower total resistance of 207 Ω at −20 °C. In the case of the f-EA electrolyte, it showed the highest total resistance of 375 Ω at −20 °C; presumably due to low $Li^+$ ion solubility and ionic conductivity at low temperatures (Figure S11, Supporting Information).

To compare each resistance component contribution, we deconvoluted and extracted the charge transfer resistance at the anode ($R_{ct\text{-}anode}$) and charge transfer resistance at the cathode ($R_{ct\text{-}cathode}$) from the measured data, since those two components are known as limiting factors at low temperatures (Figure 4e,f). The EIS data were well fitted with the equivalent circuit at −15 °C, verifying the fitting model (Figure S12, Supporting Information), and the fitting results of parameters are provided in Tables S2–S5 (Supporting Information). In the Arrhenius plot of $R_{ct\text{-}anode}$, Gen 2 showed the lowest resistance due to the ion-conductive SEI layer derived from EC reduction. While the EA electrolyte showed the highest resistance, EA-f and EA-f with LiDFOB additive showed relatively low resistances, likely due to the weaker solvation structure and modified SEI layer. In the case of $R_{ct\text{-}cathode}$, since there was no major difference in CEI layer composition, the weaker solvation effect was directly observed. While EA electrolyte showed similar resistances to Gen 2, EA-f and EA-f with LiDFOB additive showed much smaller resistances. The temperature-dependent EIS measurement shows that the weak solvation structures in EA-f electrolytes improve the interfacial kinetics with the support of a modified SEI layer.

### 2.4. Electrochemical Performances

One of the advantages of fluorination is high oxidation stability. To compare the stability of electrolytes, we conducted

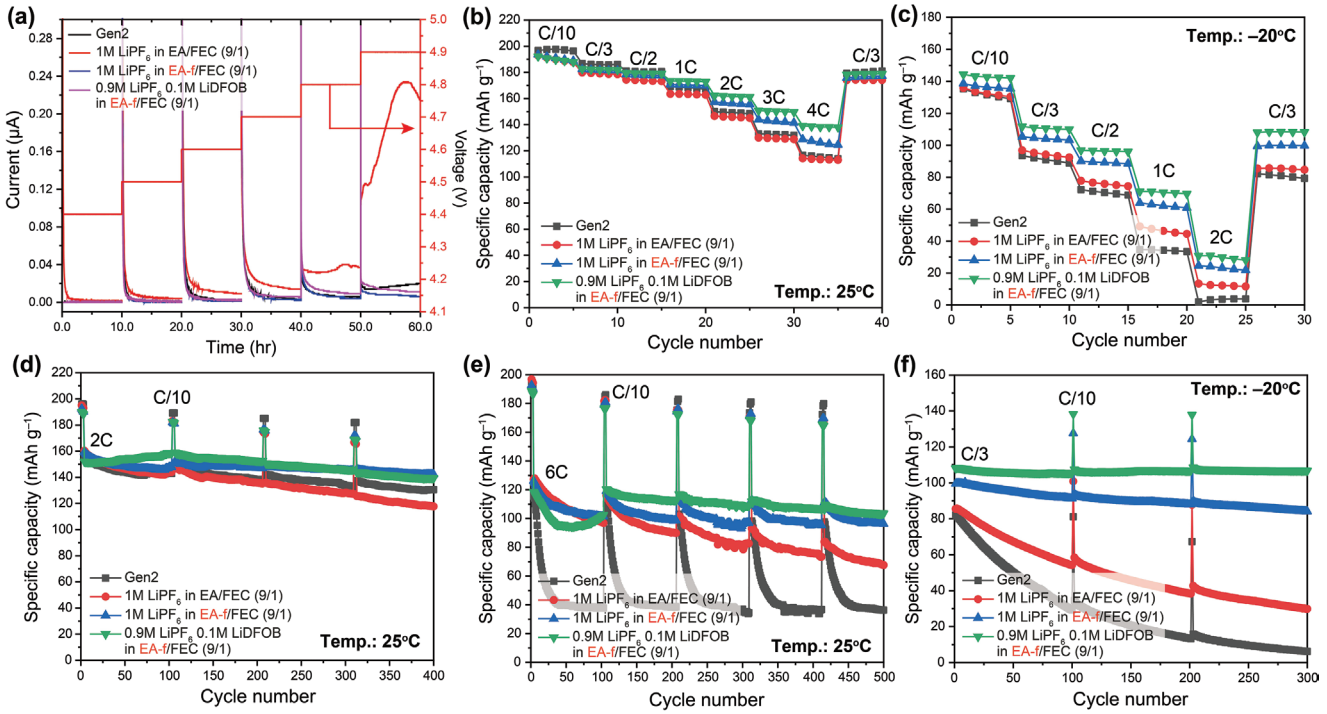


**Figure 5.** a) Voltage holding test of graphite|NMC622 cells with different electrolytes from 4.4 to 4.9 V. C-rate capability with different electrolytes at: b) 25 °C and c) −20 °C. Cyclability at: d) 2 C and e) 6 C rate with different electrolytes at 25 °C. f) Cyclability at C/3 rate with different electrolytes at −20 °C.

a voltage holding test of NMC622/graphite cells with different electrolytes with a voltage holding from 4.4 to 4.9 V for 10 h in each step (**Figure 5**a). For Gen 2, the leakage current sustained low up to 4.8 V, but started slightly increasing at 4.9 V. While the EA electrolyte showed a leakage current above 4.6 V and rapidly increases at 4.9 V, EA-f and EA-f with LiDFOB additive maintained a low leakage current up to 4.9 V, indicating their superior oxidation stability. The trend of leakage currents was continued in NMC622/Li metal cells (Figure S13, Supporting Information). These results suggest the application of EA-f electrolytes for high voltage cathodes such as $LiNi_{0.5}Mn_{1.5}O_4$.

We measured rate capability of electrolytes at 25 °C and −20 °C (Figure 5b,c). Note that the EA-f electrolytes showed lower initial capacities than Gen 2 due to lower CEs for the formation cycles (Figure S14, Supporting Information). At room temperature, when various C-rates were applied from C/10 to 4 C, Gen 2 and EA electrolyte showed similar capacities of 116 and 113 $mAhg^{-1}$ at 4 C, respectively. In contrast, EA-f electrolyte with LiDFOB additive showed the best rate capability and delivered 138 $mAhg^{-1}$ at 4 C due to the weak solvation structure and modified SEI layer. As shown in the voltage profiles with normalized capacity (Figure S15, Supporting Information), the overpotential evolution of Gen 2 approached 0.62 V at 4 C, whereas that of EA-f electrolyte with LiDFOB additive maintained a low overpotential of 0.4 V at 4 C.

When the temperature dropped to −20 °C, the difference in rate capability between the electrolytes was further diverged. When a current of 1 C was applied at −20 °C, Gen 2 only exhibited 33 $mAhg^{-1}$ capacity, while EA-f electrolyte with LiDFOB additive still maintained a high capacity of 70 $mAhg^{-1}$. In the voltage profiles of rate capabilities at −20 °C (Figure S16, Supporting Information), Gen 2 showed a high overpotential of 1.1 V at 1 C while the EA-f electrolyte with LiDFOB additive remained at 0.77 V at 1 C. To exclude the effect of high ion-pair ratio in electrolytes, we tested 2 and 3 M EA electrolytes with same test conditions (Figure S17, Supporting Information), and in the case of 3 M EA electrolyte, it showed better rate capability than Gen 2 at 25 °C, but poor capability at −20 °C due to the ion clustering and low ionic conductivity. Poor performance was also observed in f-EA electrolyte (Figure S18, Supporting Information), reconfirming the trade-off relation between the weak solvation structure and electrochemical performance. Finally, superior rate capabilities of EA-f electrolytes were demonstrated in Li metal batteries (Figure S19, Supporting Information), showing the best capacity retention at 25 °C and −20 °C.

Long-term cyclability at high C-rates and low temperatures is considered as one of the challenging aspects for LIBs. To prove the superiority of our electrolytes, we conducted long-term cycling tests with various conditions (Figure 5d–f). When a current of 2 C was applied at 25 °C, the EA electrolyte gradually decayed to a capacity retention of 73% after 400 cycles, while the EA-f electrolyte with LiDFOB additive showed the best capacity retention of 91% after 400 cycles. This trend continues at a further high current of 6 C. While Gen 2 rapidly degraded to 34% within 50 cycles, the EA-f electrolyte with LiDFOB additive showed the best capacity retention of 85% even after 500 cycles. When a current of C/3 was applied at −20 °C, Gen 2 and EA electrolytes showed a severe capacity degradation, corresponding to 7.5% and 34% capacity retention after 300 cycles, respectively. In stark contrast, the EA-f electrolyte

with LiDFOB additive showed a negligible capacity loss and retained 97% capacity even after 300 cycles. In addition, in all test conditions, the Coulombic efficiencies (Ces) of the EA-f electrolyte with LiDFOB additive were higher than those of other electrolytes (Figure S20, Supporting Information). This cycling test result reveals the superior stability of our electrolyte for fast charging and low temperature operations.

## 3. Conclusions

In summary, we have systematically investigated the effect of the position and degree of fluorination in EA solvent on electrochemical performances. We reveal that a high degree of fluorination or fluorination close to ester group imposes more electron-withdrawing effect, resulting in low atomic charges, low binding energies to $Li^+$ ions, low ionic conductivities, and poor solubilities at low temperatures. Since interfacial resistance is governed by the kinetics of $Li^+$ ion desolvation, charge transfer across the SEI and ion conductivity, EA-f electrolyte shows the best electrochemical performance at subzero temperature. EA-f effectively balances the property trade-offs associated with fluorination, outperforming both f-EA- and f-EA-f-based electrolytes. This study provides a deep insight on design principles of novel fluorinated electrolytes for LIBs operating at low temperatures.

## 4. Experimental Section

*Materials*: Ethyl acetate (EA), trifluoroethyl acetate (EA-f), ethyl trifluoroacetate (f-EA), and trifluoroethyl trifluoroacetate (f-EA-f) were purchased from Sigma Aldrich. All solvents used in this study were purified by vacuum distillation and then dried by adding 4 Å molecular sieves before use. Gen2 electrolyte was 1.2 M $LiPF_6$ in EC/EMC (3/7 = w/w ratio). All electrodes were provided by Argonne's Cell Analysis, Modeling and Prototyping (CAMP) facility. The cathode NMC622 was composed of 90 wt% $LiNi_{0.6}Mn_{0.2}Co_{0.2}O_2$, 5 wt% polyvinylidene fluoride binder (PVdF, Solvay), and 5 wt% C45 conductive carbon casted on an aluminum foil with a mass loading of 9.78 mg $cm^{-2}$. The graphite anode was composed of 91.83 wt% superior graphite (SLC1520P), 6 wt% PVdF binder (Kureha, 9300), 0.17 wt% oxalic acid additive, and 2 wt% C45 conductive carbon casted on a copper foil with a mass loading of 6.38 mg $cm^{-2}$. All electrodes were dried at 110 °C under vacuum for overnight. Celgard 2500 was used as the separator. The diameters of the cathode, anode, and separator were 14, 15, and 16 mm, respectively.

*Electrochemical Measurements*: The electrochemical performance was evaluated by 2032-coin cells. The full cells were composed of NMC622 cathode and graphite anode with different electrolytes. The cell assembly was conducted in an argon-filled glovebox. All the galvanostatic cycling was performed at 2.7– 4.4 V following three C/10 formation cycles using Neware battery tester. The electrochemical impedance spectroscopy (EIS) was obtained and fitted using a Solartron analyzer operated between 0.01 and 1 MHz with amplitude of 10 mV.

*Characterization*: The cycled cells were disassembled in an argon-filled golvebox. The graphite and NMC622 electrodes were obtained at charged state to 3.7 V after three formation cycles with Gen 2, EA, EA-f, and LiDFOB-added EA-f electrolytes. The electrodes were rinsed with dimethyl carbonate for Gen 2 cycled electrodes or EA for EA, EA-f, and LiDFOB-added EA-f electrolytes, and characterized after vacuum dried. X-ray photoelectron spectroscopy (XPS) was conducted in the fixed analyzer transmission mode using an Al K$\alpha$ radiation ($h\nu$ = 1486.6 eV, 100 µm beam, 25 W) with $Ar^+$ and electron beam sample neutralization. XPS spectra were calibrated to the C—C bond at 284.7 eV.

*DFT Calculation*: Structure optimizations, binding energy, and molecular orbital energy calculations were performed without symmetry restriction using the B3LYP hybrid density functional implemented in the Gaussian 16 software package. The 6–311+G(d) basis sets were used for all the atoms. Frequency calculations of the same basis sets were conducted to obtain Gibbs free energies of the solvents. The atomic charge was obtained from the natural bond orbital (NBO) analysis. The conductor-like polarization continuum model (CPCM) with the dielectric constant ($\varepsilon$ = 6.02) was used to implicitly take included solvent molecules into consideration. The reduction or oxidation potentials were calculated based on the following equation:

$$E\left(\text{vs Li}/\text{Li}^+\right) = \frac{\Delta G}{-nF} - 1.4 \quad (1)$$

where $E$ is the formal potential, $\Delta G$ is the free energy of reaction, $n$ is the number of electrons transferred in the reaction, and $F$ is Faraday's constant. The potential compared $Li/Li^+$ was determined by subtracting 1.4 V, because the SHE is –4.4 V versus vacuum and the potential of $Li/Li^+$ is –3.0 V versus SHE.

*MD Simulation*: The system was parameterized with the Sage force field[40] using the OpenForceField toolkit. Partial charges for FEC and the esters were calculated with AM1-BCC, the recommended charge method for Sage.[41] $PF_6^-$ could not be parameterized with AM1-BCC, so the authors instead used the $PF_6^-$ partial charges used.[8,42] Following prior works, partial charges for $Li^+$ and $PF_6^-$ partial charges were scaled to 80% of their initial value to account for the lack of electronic polarization.[35,43,44]

Molecular dynamics calculations were performed with the Open Molecular Mechanics (OpenMM) package.[45] Simulations were set up with a different EAx/FEC ratio and different numbers of $LiPF_6$ to maintain a 9/1 v/v ratio and 1 M $LiPF_6$ (Table S6, Supporting Information). A random initial configuration of the molecular system was generated with PACKMOL,[46] followed by an energy minimization with conjugate gradient descent. Each simulation began with a 1 ns pressure equilibration in the NPT ensemble at 1 atm, 298 K. The system was then annealed by raising the temperature to 400 K, holding at 400 K, and then returning to 298 K, each for 1 ns. After this equilibration, the production part of the simulation ran for 5 ns. Additional configuration parameters were shown in Table S7 (Supporting Information). All solvation structure geometries and statistics were taken from the production run. Simulation setup was performed with Pymatgen[47] and analysis of the molecular dynamics trajectories with MD Analysis[48] and Solvation Analysis.[49]

## Supporting Information

Supporting Information is available from the Wiley Online Library or from the author.

## Acknowledgements

This work was funded by the U.S. Department of Energy (DOE), Office of Energy Efficiency and Renewable Energy, Vehicle Technologies Office. Support from Peter Faguy and Mallory Clites of Office of Vehicle Technology Office is gratefully acknowledged. The submitted manuscript has been created by UChicago Argonne, LLC, Operator of Argonne National Laboratory, which is supported by DOE Office of Science under Contract No. DE-AC02-06CH11357.

## Conflict of Interest

The authors declare no conflict of interest.

## Data Availability Statement

Research data are not shared.

## Keywords

fluorinated esters, lithium-ion batteries, low temperature performance, nonaqueous electrolytes

Received: December 7, 2022
Revised: March 7, 2023
Published online: April 9, 2023

[1] J. W. Choi, D. Aurbach, *Nat. Rev. Mater.* **2016**, *1*, 16013.
[2] F. Duffner, N. Kronemeyer, J. Tübke, J. Leker, M. Winter, R. Schmuch, *Nat. Energy* **2021**, *6*, 123.
[3] M. Li, J. Lu, Z. Chen, K. Amine, *Adv. Mater.* **2018**, *30*, 1800561.
[4] X. Zeng, M. Li, D Abd El-Hady, W. Alshitari, A. S. Al-Bogami, J. Lu, K. Amine, *Adv. Energy Mater.* **2019**, *9*, 1900161.
[5] A. Gupta, A. Manthiram, *Adv. Energy Mater.* **2020**, *10*, 2001972.
[6] J. Hou, M. Yang, D. Wang, J. Zhang, *Adv. Energy Mater.* **2020**, *10*, 1904152.
[7] G. Zhu, K. Wen, W. Lv, X. Zhou, Y. Liang, F. Yang, Z. Chen, M. Zou, J. Li, Y. Zhang, W. He, *J. Power Sources* **2015**, *300*, 29.
[8] D.-J. Yoo, Q. Liu, O. Cohen, M. Kim, K. A. Persson, Z. Zhang, *ACS Appl. Mater. Interfaces* **2022**, *14*, 11910.
[9] H.-Y. Song, S.-K. Jeong, *J. Power Sources* **2018**, *373*, 110.
[10] J. Ming, Z. Cao, Y. Wu, W. Wahyudi, W. Wang, X. Guo, L. Cavallo, J.-Y. Hwang, A. Shamim, L.-J. Li, Y.-K. Sun, H. N. Alshareef, *ACS Energy Lett.* **2019**, *4*, 2613.
[11] X.-Z. Liao, Z.-F. Ma, Q. Gong, Y.-S. He, L. Pei, L.-J. Zeng, *Electrochem. Commun.* **2008**, *10*, 691.
[12] M. C. Smart, B. V. Ratnakumar, L. D. Whitcanack, K. B. Chin, S. Surampudi, H. Croft, D. Tice, R. Staniewicz, *J. Power Sources* **2003**, *119–121*, 349.
[13] L. Carbone, M. Gobet, J. Peng, M. Devany, B. Scrosati, S. Greenbaum, J. Hassoun, *ACS Appl. Mater. Interfaces* **2015**, *7*, 13859.
[14] Q. Zhao, X. Liu, J. Zheng, Y. Deng, A. Warren, Q. Zhang, L. Archer, *Proc. Natl. Acad. Sci. USA* **2020**, *117*, 26053.
[15] J. Xu, X. Wang, N. Yuan, J. Ding, S. Qin, J. M. Razal, X. Wang, S. Ge, Y. Gogotsi, *Energy Storage Mater.* **2019**, *23*, 383.
[16] H. V. Ramasamy, S. Kim, E. J. Adams, H. Rao, V. G. Pol, *Chem. Commun.* **2022**, *58*, 5124.
[17] X. Zhang, L. Zou, Y. Xu, X. Cao, M. H. Engelhard, B. E. Matthews, L. Zhong, H. Wu, H. Jia, X. Ren, P. Gao, Z. Chen, Y. Qin, C. Kompella, B. W. Arey, J. Li, D. Wang, C. Wang, J.-G. Zhang, W. Xu, *Adv. Energy Mater.* **2020**, *10*, 2000368.
[18] Y. Qin, Z. Ren, Q. Wang, Y. Li, J. Liu, Y. Liu, B. Guo, D. Wang, *ACS Appl. Mater. Interfaces* **2019**, *11*, 27854.
[19] M. C. Smart, B. V. Ratnakumar, S. Surampudi, *J. Electrochem. Soc.* **2002**, *149*, A361.
[20] S. Herreyre, O. Huchet, S. Barusseau, F. Perton, J. M. Bodet, P. Biensan, *J. Power Sources* **2001**, *97–98*, 576.
[21] S. V. Sazhin, M. Y. Khimchenko, Y. N. Tritenichenko, H. S. Lim, *J. Power Sources* **2000**, *87*, 112.
[22] W. Lu, K. Xie, Z. Chen, S. Xiong, Y. Pan, C. Zheng, *J. Power Sources* **2015**, *274*, 676.
[23] K. A. Smith, M. C. Smart, G. K. S. Prakash, B. V. Ratnakumar, *ECS Trans.* **2008**, *11*, 91.
[24] W. Lu, K. Xie, Y. Pan, Z.-x. Chen, C.-m. Zheng, *J. Fluor. Chem.* **2013**, *156*, 136.
[25] M. C. Smart, B. V. Ratnakumar, K. B. Chin, L. D. Whitcanack, *J. Electrochem. Soc.* **2010**, *157*, A1361.
[26] Y.-G. Cho, Y.-S. Kim, D.-G. Sung, M.-S. Seo, H.-K. Song, *Energy Environ. Sci.* **2014**, *7*, 1737.
[27] J. Chen, J. Vatamanu, L. Xing, O. Borodin, H. Chen, X. Guan, X. Liu, K. Xu, W. Li, *Adv. Energy Mater.* **2020**, *10*, 1902654.
[28] L. Hu, Z. Zhang, K. Amine, *Electrochem. Commun.* **2013**, *35*, 76.
[29] A. Tornheim, R. Sahore, M. He, J. R. Croy, Z. Zhang, *J. Electrochem. Soc.* **2018**, *165*, A3360.
[30] Z. Zhang, L. Hu, H. Wu, W. Weng, M. Koh, P. C. Redfern, L. A. Curtiss, K. Amine, *Energy Environ. Sci.* **2013**, *6*, 1806.
[31] J. Holoubek, M. Yu, S. Yu, M. Li, Z. Wu, D. Xia, P. Bhaladhare, M. S. Gonzalez, T. A. Pascal, P. Liu, Z. Chen, *ACS Energy Lett.* **2020**, *5*, 1438.
[32] K. Sato, I. Yamazaki, S. Okada, J.-i. Yamaki, *Solid State Ion* **2002**, *148*, 463.
[33] Y. Yang, P. Li, N. Wang, Z. Fang, C. Wang, X. Dong, Y. Xia, *Chem. Commun.* **2020**, *56*, 9640.
[34] K. An, Y. H. T. Tran, S. Kwak, J. Han, S.-W. Song, *Adv. Funct. Mater.* **2021**, *31*, 2106102.
[35] T. Hou, K. D. Fong, J. Wang, K. A. Persson, *Chem. Sci.* **2021**, *12*, 14740.
[36] J.-P. Jones, M. C. Smart, F. C. Krause, R. V. Bugga, *J. Electrochem. Soc.* **2020**, *167*, 020536.
[37] M. Xu, L. Zhou, L. Hao, L. Xing, W. Li, B. L. Lucht, *J. Power Sources* **2011**, *196*, 6794.
[38] L. Xia, S. Lee, Y. Jiang, Y. Xia, G. Z. Chen, Z. Liu, *ACS Omega* **2017**, *2*, 8741.
[39] S. Li, Q. Liu, W. Zhang, L. Fan, X. Wang, X. Wang, Z. Shen, X. Zang, Y. Zhao, F. Ma, Y. Lu, *Adv. Sci.* **2021**, *8*, 2003240.
[40] Y. Qiu, D. G. A. Smith, S. Boothroyd, H. Jang, D. F. Hahn, J. Wagner, C. C. Bannan, T. Gokey, V. T. Lim, C. D. Stern, A. Rizzi, B. Tjanaka, G. Tresadern, X. Lucas, M. R. Shirts, M. K. Gilson, J. D. Chodera, C. I. Bayly, D. L. Mobley, L.-P. Wang, *J. Chem. Theory Comput.* **2021**, *17*, 6262.
[41] A. Jakalian, D. B. Jack, C. I. Bayly, *J. Comput. Chem.* **2002**, *23*, 1623.
[42] T. Hou, G. Yang, N. N. Rajput, J. Self, S.-W. Park, J. Nanda, K. A. Persson, *Nano Energy* **2019**, *64*, 103881.
[43] A. J. Ringsby, K. D. Fong, J. Self, H. K. Bergstrom, B. D. McCloskey, K. A. Persson, *J. Electrochem. Soc.* **2021**, *168*, 080501.
[44] M. I. Chaudhari, J. R. Nair, L. R. Pratt, F. A. Soto, P. B. Balbuena, S. B. Rempe, *J. Chem. Theory Comput.* **2016**, *12*, 5709.
[45] P. Eastman, J. Swails, J. D. Chodera, R. T. McGibbon, Y. Zhao, K. A. Beauchamp, L.-P. Wang, A. C. Simmonett, M. P. Harrigan, C. D. Stern, R. P. Wiewiora, B. R. Brooks, V. S. Pande, *PLoS Comput. Biol.* **2017**, *13*, e1005659.
[46] L. Martínez, R. Andrade, E. G. Birgin, J. M. Martínez, *J. Comput. Chem.* **2009**, *30*, 2157.
[47] S. P. Ong, W. D. Richards, A. Jain, G. Hautier, M. Kocher, S. Cholia, D. Gunter, V. L. Chevrier, K. A. Persson, G. Ceder, *Comput. Mater. Sci.* **2013**, *68*, 314.
[48] R. J. Gowers, M. Linke, J. Barnoud, T. J. E. Reddy, M. N. Melo, S. L. Seyler, D. L. Dotson, J. Domanski, S. Buchoux, I. M. Kenney, O. Beckstein, in S. Benthall, S. Rostrup (Eds.), *Proceedings of the 15th Python in Science Conference*, **2016**. Sc, iPy, Austin, TX, pp. 98–105.
[49] O. Cohen, Solvation Analysis v0.1.2, **2021**. https://pypi.org/project/solvation-analysis/.